Ultrathin two-dimensional BiOBr$_x$I$_{1-x}$ solid solution with rich oxygen vacancies for enhanced visible-light-driven photoactivity in environmental remediation

Qiao Wang[a], Zhiquan Liu[a], Dongmei Liu[a], Guoshuai Liu[a], Min Yang[b], Fuyi Cui[a,c,**], Wei Wang[a,*]

[a] State Key Laboratory of Urban Water Resource and Environment, School of Environment, Harbin Institute of Technology, Harbin, 150090, PR China
[b] MIIT Key Laboratory of Critical Materials Technology for New Energy Conversion and Storage, School of Chemistry and Chemical Engineering, Harbin Institute of Technology, Harbin, 150001, PR China
[c] College of Urban Construction and Environmental Engineering, Chongqing University, Chongqing, 400044, PR China

ARTICLE INFO

ABSTRACT

Photocatalysis is intensively investigated for environmental remediation, but suffering from moderate efficiency toward the colorless persistent organic contaminants, the major category of organic pollutants in water environment. Herein, a novel series of oxygen vacancy-rich ultrathin two-dimensional BiOBr$_x$I$_{1-x}$ solid solution nanosheets (BBI-x) were successfully constructed via a one-step solvothermal method. Under visible light irradiation, the optimal BiOBr$_{0.85}$I$_{0.15}$ sample (BBI-0.85) exhibited over 90% degradation efficiency of 4-chlorophenol (4-CP) within 30 min, which was 4.4, 10.9 and 5.9 times greater than that of pure BiOI nanosheets, pure BiOBr nanosheets and oxygen vacancy-poor BiOBr$_{0.85}$I$_{0.15}$ nanoplates, respectively. Also, this excellent photoactivity can expand to other colorless organic contaminants, such as bisphenol analogues and sulfonamides, verifying the universal applicability of BiOBr$_x$I$_{1-x}$. The enhanced activity can be ascribed to the synergistic effect of solid solution and oxygen vacancies. Formation of solid solution promotes visible-light harvesting and photogenerated charge carriers' separation efficiency, as well as endows photoinduced holes with sufficient oxidation capacity, unambiguously confirmed by multiple optical and photoelectrochemical characterizations. Meanwhile, the oxygen vacancies induce an intermediate level near the Fermi level, narrowing the band gap energy and impeding the recombination of photogenerated charge carriers, as evidenced by density functional theory (DFT) analyses. This work could give ideas for the design of highly active photocatalysts toward sustainable solar-to-chemical energy conversion and environmental remediation.

1. Introduction

Semiconductor photocatalysis technology has attracted tremendous interest as an efficient and green method to degrade recalcitrant organic pollutants in water environment [1–3]. To utilize sunlight effectively, it is indispensable to develop the visible-light-responsive (VLR) photocatalysts [4,5]. Theoretically, high active VLR photocatalysts require three aspects: i) wide and efficient absorption of visible light to generate an abundance of charge carriers; ii) quickly separation of charge carriers to minimize recombination; iii) sufficient high conduction band (CB) and valence band (VB) energy to endow charge carriers with adequate reduction and oxidation potential [6–8]. Nevertheless, widening absorption spectrum and acquiring high CB and VB energy are conflicting in pristine semiconductor materials [9].

Accordingly, various strategies, such as Z-scheme heterostructures [10,11], doping [12], solid solutions [6,13,14], deposition of noble metals [15], and so on, have been employed to overcome this conflict. Among them, stimulated by the continuous modulation of band structure, great interest has emerged in solid solution photocatalysts.

Solid solution enables to achieve the balance between light absorption and redox capability. In detail, it can narrow the band gap (Eg) to absorb visible light in a wide spectrum, as well as increase the level of conduction band minimum (CBM) or decreasing the level of valence band maximum (VBM), or both, to enhance the redox capability [6]. More recently, some researchers have constructed solid solution to improve their photocatalytic activities. Zhang and co-workers developed Zn$_x$Cd$_{1-x}$S solid solution photocatalyst for methylene blue degradation under visible light irradiation [16]. Yu and co-workers

---

* Corresponding author.
** Corresponding author at: State Key Laboratory of Urban Water Resource and Environment, School of Environment, Harbin Institute of Technology, Harbin, 150090, PR China.
E-mail addresses: cuifuyi@hit.edu.cn (F. Cui), wangweirs@hit.edu.cn (W. Wang).

demonstrated that BiOCl$_x$Br$_{1-x}$ solid solution nanoplates exhibited high activities in photocatalytic Rhodamine B degradation [17]. Nevertheless, the previous study mainly focused on the activity of solid solution materials in photooxidation of sensitized organic dye [16–19], and photoreduction of water [20], CO$_2$ and heavy metals [14], while the application in oxidizing colorless organic contaminants without sensitization under visible light irradiation is still in its infancy and unsatisfactory. Precisely, these colorless organic contaminants are a major category of pernicious pollutants in water environment. Thus, there exists a strong need and great significant to develop approaches to further enhance the photooxidation performance of solid solution materials to degrade colorless organic contaminants.

Very recently, the defect engineering is recognized as an effective method to improve the catalytic activity of materials in both energy and environment-related application [21–24]. Constructing two-dimensional (2D) ultrathin nanosheets enables vast interior atoms to be exposed and inevitably induces the formation of defects with structure disorder on their surfaces [25]. Accordingly, we attempted to fabricate 2D ultrathin solid solution nanosheets, and hypothesized that better photooxidation activity can be achieved. Noteworthily, among numerous semiconductor materials, bismuth oxyhalide (BiOX, X = F, Cl, Br or I) easily crystallizes into anisotropic 2D nanosheets or nanoplates, due to its unique layered structure comprising a layer of [Bi$_2$O$_2$]$^{2+}$ slab interleaved by double slabs of halogen atoms [26].

Herein, in this work, we design an oxygen vacancy (OV)-rich ultrathin BiOBr$_x$I$_{1-x}$ solid solution nanosheet (~3.6 nm thickness) as a model material to study its photocatalytic activities to colorless organic contaminants and the impacts of solid solution and vacancy on photocatalytic activities. These OV-rich BiOBr$_x$I$_{1-x}$ nanosheets were synthesized via a facile solvothermal method, and their visible-light photoactivity were evaluated by the degradation of 4-chlorophenol (4-CP), which was selected as a colorless probe organic contaminant. The optimal BiOBr$_{0.85}$I$_{0.15}$ sample exhibited over 90% degradation efficiency of 4-CP within 30 min visible light irradiation, and it possessed a universal excellent photocatalytic activity to other colorless persistent organic contaminants. Furthermore, the possible mechanism for enhanced photocatalytic performance was elucidated by experimental and theoretical calculation results, which was benefited from the synergistic effect of oxygen vacancies and solid solution. Last, a possible photocatalytic degradation pathway of 4-CP was also proposed. It is believed that the introduction of ultrathin solid solution materials could bring new opportunities for photocatalysis, environmental restoration and other applications.

2. Experimental section

2.1. Materials

All chemical reagents used in this work were analytical reagent grade and without further purification. Bismuth nitrate pentahydrate (Bi(NO$_3$)$_3$·5H$_2$O), sodium bromide (NaBr), potassium iodide (KI), polyvinylpyrrolidone (PVP, K-30), glycerol, 4-chlorophenol (4-CP) and ethanol were purchased from Sinopharm Chemical Reagent Co. Ltd. Deionized water was used throughout the experiments.

2.2. Catalysts preparation

2.2.1. Synthesis of oxygen vacancy-rich ultrathin BiOBr$_x$I$_{1-x}$ (BBI-x) nanosheets

In a typical procedure, 0.486 g of Bi(NO$_3$)$_3$·5H$_2$O and 0.400 g PVP were added in 25 mL water at room temperature without stirring. Then, 25 mL glycerol were poured into this mixture with vigorous stirring for 1 h, yielding a transparent mixture solution. A total of 1.0 mmol NaBr and KI with different molar ratios was dissolved into 5 mL water, and then this solution was dropwise added into the above mixture. After another 30 min of agitation, the mixture solution was transferred into a

100 mL Teflon-lined stainless steel autoclave. The autoclave was heated at 160 °C for 6 h under autogenous pressure, and then cooled to room temperature naturally. Finally, the resulting product was gathered by centrifugation, washed three times with water and dried at 50 °C. The obtained samples were denoted as BBI-x, where x referred to the micromolar amount of NaBr (x = 1, 0.95, 0.85, 0.75, 0.5, 0), which could be abbreviated as BB, BBI-0.95, BBI-0.85, BBI-0.75, BBI-0.5 and BI.

2.2.2. Synthesis of oxygen vacancy-poor BiOBr$_x$I$_{1-x}$ nanoplates

As a control sample, the BiOBr$_{0.85}$I$_{0.5}$ nanoplates with poor oxygen vacancies were synthesized in a similar way without adding PVP, and denoted as BBI-P.

2.3. Characterization

To identify the material composition and the crystal phase of BiOBr$_x$I$_{1-x}$ samples, XRD patterns were collected by using a Bruker D8 X-ray diffractometer with Cu Ka radiation (λ = 0.15418 nm). The micro-morphologies of the samples were obtained from the Quanta 200FEG SEM, FEI Tecnai G2 F30 TEM and JEOL JEM-1400 TEM. The thickness of the samples was determined by atomic force microscopy (AFM, Bioscope system, USA). The BET surface area measurements were recorded on an ASAP2020 instrument. X-ray photoelectron spectroscopy measurements were performed by a Thermo ESCALAB 250 with Al Kα X-ray (hν = 1486.6 eV) radiation. Electron spin resonance (ESR) spectroscopy (Bruker A300 spectrometer, Germany) were used to investigate the existence of oxygen vacancies and the generation of reactive radicals. The UV–vis diffuse reflectance spectra (DRS) of samples were obtained by a spectrophotometer (Shimadzu, UV2550), using the BaSO$_4$ as the reflectance sample. The steady-state photoluminescence (PL) spectra were detected by using an Hitachi F-4600 fluorescence spectrophotometer with excitation at 325 nm. The time-resolved fluorescence emission decay spectra were recorded on an ISS ChronosBH time-domain fluorescence spectrophotometer.

2.4. Photocatalytic activity measurement

The visible-light-driven photocatalytic activity of all the samples were estimated by measuring the degradation of 4-chlorophenol (4-CP). A 300 W short-arc xenon lamp (Perkin-Elmer, PE300BF) equipped with a 420 nm cut-off filter was used as the light source. The reactor was made of open cylindrical Pyrex with diameter 4.5 cm and height 8 cm. The distance between the light source and the surface of the solute was approximately 20 cm. In a typical photocatalytic experiment, 50 mg of sample was dispersed in 100 mL of 4-CP solution (10 mg/L). Before the light irradiation, the mixture was stirred for 30 min to reach the adsorption equilibrium in the dark. The temperature of the reactor was maintained at 20 °C by continuous circulating water. At given irradiation time intervals, about 2 mL of the solution was taken out to analyze the residual contaminant concentration.

The concentration of 4-CP was detected by the HPLC system (Waters Baseline 810) with a Waters 486 tunable UV absorbance detector and a Supelco LC-18-DB column (250 mm × 4.6 mm). The HPLC separations were carried out at 280 nm with a mixture of acetonitrile and water in a volume ratio of 55:45 at a flow rate of 1 mL min^{-1}. The concentration of chloride ion was analyzed by the ion chromatography (ICS2100).

To investigate the universal applicability of BBI-0.85 sample, several bisphenol analogues (bisphenol A (BPA), bisphenol F (BPF) and bisphenol S (BPS)) and sulfonamides (sulfadiazine (SDZ) and sulfamerazine (SMZ)) were also degraded in the similar condition of 4-CP, and their concentrations were also analyzed by HPLC. The HPLC separations of BPA and BPF were detected at 230 nm with a mixture of methanol and water in a volume ratio of 60:40 at a flow rate of 1 mL min^{-1}. The HPLC separations of BPS was detected at 260 nm with a mixture of acetonitrile and water in a volume ratio of 30:70 at a flow rate of 1 mL min^{-1}. The HPLC separations of SDZ and SMZ were

detected at 265 nm with a mixture of acetonitrile and 0.1% formic acid in water in a volume ratio of 30:70 at a flow rate of 1 mL min^{-1}.

The intermediate products of 4-CP degradation were detected by an Ultra Performance Liquid Chromatography tandem mass spectrometry (UPLC-MS, Acquity UPLC-MS) with a triple quadrupole detector (Xevo TQ-S). The negative mode electrospray ionization ((-) ESI) was conducted to analyze the mass spectra. A 10 μL volume was injected, and the mobile phase was a mixture of acetonitrile and water with a volume ratio of 55:45 at a flow rate of 0.1 mL min^{-1}.

2.5. Photoelectrochemical measurement

The transient photo-current measurements and electrochemical impedance spectroscopy (EIS) were recorded in a three-electrode quartz cell by using an Electrochemical Workstation (660E, Shanghai Chenhua, China). The 0.5 M Na$_2$SO$_4$ aqueous solution was used as the electrolyte. The fabricated photoanodes, a Pt foil, and calomel electrode were used as working, counter and reference electrode, respectively. The working electrodes were prepared by spin-coating method. 5 mg of the photocatalyst powder was suspended in 5 mL of anhydrous ethanol to produce suspension by sonication for 1 h. And then the suspension was spin-coated (2000 rpm) onto ITO glass supports as the working electrode. A short-arc xenon lamp (Perkin-Elmer, PE300BF) with a cutoff filter (λ ≥ 420 nm) was used as the visible-light source. The power intensity of the incident light was adjusted to 100 mW·cm^{-2} by a Si photodiode (Thor Labs).

2.6. Theoretical calculations

Our calculations were performed using the periodic density functional theory (DFT) package of Cambridge Serial Total Energy Package (CASTEP) codes. The Perdew-Burke-Ernzerhof (PBE) functional of the generalized gradient approximation (GGA) was used as the exchange-correlation function. The core electrons were treated with the ultrasoft pseudopotential. The $2 \times 2 \times 2$ tetragonal BiOX (X = Br or I) supercell (Space group tP6, 129) was built containing 56 atoms and the next calculation process based on this structure. An energy cutoff of 420 eV and a Monkhorst-Pack k-point meshes of $3 \times 3 \times 1$ were proposed to carry out geometry optimization and electronic structure calculation. The energy, atomic displacement, stress and force convergence criteria were set as 5×10^{-6} eV per atom, 5×10^{-4} Å, 0.02 GPa and 0.01 eV Å^{-1}, respectively. For ultrathin BBI-0.85 sample, two bromine atoms in the BiOBr supercell were substituted with iodine atoms to simulate BiOBr$_{0.85}$I$_{0.15}$ solid solution, and two oxygen atoms were removed to construct oxygen vacancies. In contrast, as for BBI-P, two bromine atoms were also replaced by iodine atoms without removing oxygen atoms.

3. Results and discussion

3.1. Morphology and structure

X-ray powder diffraction (XRD) was carried out to investigate the crystal phase of the as-prepared samples. Fig. 1a shows the XRD patterns of the samples with different x values (x = 1, 0.95, 0.85, 0.75, 0.5, 0). When x is set as 1 and 0, the as-prepared samples are pure BiOBr and BiOI, whose diffraction peaks are well indexed as the standard diffraction patterns of tetragonal BiOBr (PDF#73-2061) and tetragonal BiOI (PDF#10-0445), respectively. Remarkably, as shown in the enlarged XRD patterns (Fig. 1b), when an increasing amount of Br is substituted by I in the BiOBr crystal, the diffraction peaks significantly shift toward lower angles, resulting from the larger radius of I$^-$ with respect to Br$^-$ [6,14]. These results indicate that the as-fabricated BBI-x samples are solid solutions rather than compounds intermediary between BiOBr and BiOI.

Fig. 2 displays the morphology and element analysis of ultrathin

BBI-0.85 sample. SEM image (Fig. 2a) clearly depicts the sheet-like structure of BBI-0.85. Similarly, TEM image (Fig. 2b) also reveals the as-prepared BBI-0.85 is approximate rectangular nanosheet structure with a smooth surface, and its near-transparency indicates its ultrathin thickness [25]. From the corresponding HRTEM image (Fig. 2c), the good crystalline and clear lattice fringes can be observed, whose d-spacing is 0.281 nm, corresponding to the (110) planes of the tetragonal BiOBr$_{0.85}$I$_{0.15}$ [6]. Fig. 2d–h are the HAADF-STEM image and the corresponding EDS mapping images, it is demonstrated that bismuth, oxygen, bromine and iodine are uniformly distributed over the composite nanosheets. The thickness information of the ultrathin BBI-0.85 nanosheets is acquired from the AFM image (Fig. 2i), and the corresponding height profile is shown in the inset of Fig. 2i. As can be seen, the surface of nanosheet is relatively smooth as demonstrated by the TEM images (Fig. 2b), which can be further confirmed by the thickness fluctuation determined along the line between Point 1 (P1) and Point 2 (P2) throughout the nanosheet. The thickness of these nanosheets is estimated to be ∼3.6 nm. Therefore, all of the results mentioned above clearly revealed that the BiOBr$_{0.85}$I$_{0.15}$ ultrathin soild solution nanosheets were successfully fabricated.

X-ray photoelectron spectroscopy (XPS) was performed to investigate the surface chemical composition of samples, as shown in Fig. 3 [27]. The relevant XPS peak position is calibrated against the C 1 s peak of contaminant carbon with a binding energy of 284.8 eV. Fig. 3a shows the survey spectra of ultrathin BB, BBI-0.85 and BI nanosheets, indicating that only C, Bi, O, Br, and/or I are detected. This indicates the high purity of these samples except the slight adventitious hydrocarbons. In Fig. 3b, the peaks at 164.2 eV (Bi1) and 158.9 eV (Bi2) are observed for Bi 4f$_{5/2}$ and Bi 4f$_{7/2}$ respectively, which are characteristic of Bi^{3+} in the BiOX material [6,28]. As shown in Fig. 3c, two peaks can also be clearly identified from the Br 3d core level spectra: the band energy (Br1 peak) of 69.0 and 69.4 eV are deemed as the Br 3d$_{3/2}$, while Br2 peak located at 68.0 and 68.4 eV can be attributed to Br 3d$_{5/2}$ in BB and BBI-0.85, respectively, confirming the presence of Br$^-$ [6,14]. Similarly, in Fig. 3d, the I 3d spectra for BI and BBI-0.85 both contain two components located at 630.1 and 630.6 eV (I1) and 618.6 and 619.1 eV (I2), corresponding to I 3d$_{3/2}$ and I 3d$_{5/2}$ in BI and BBI-0.85, respectively [6,14]. Moreover, the slight shift of Br and I peaks in BBI-0.85 is probably due to the interaction between different halogen atoms[29].

Meanwhile, the oxygen-defective nature of the ultrathin BBI-0.85 nanosheets was identified by the high resolution XPS spectra of O 1 s and low-temperature ESR spectra, using BBI-P nanoplates (Fig. S1) as a reference. Fig. 3e depicts the high resolution XPS-O 1 s spectra of the two samples. The species of O2 located at 530.0 eV are originated from the lattice oxygen anions, while the species of O1 located at 531.8 and 531.4 eV belong to the oxygen vacancies (OVs) on the surface in BBI-0.85 and BBI-P samples, respectively [30,31]. Remarkably, an obviously enhancement of O1 peak can be observed in ultrathin BBI-0.85 nanosheets as compared with that of BBI-P nanoplates, demonstrating that the as-fabricated ultrathin BBI-0.85 sample have a high concentration of surface oxygen vacancies [32]. Further, the ESR spectra would provide fingerprint evidences for probing oxygen vacancies. In Fig. 3f, for BBI-0.85 nanosheets, a stronger symmetrical EPR signal at g = 2.004 appears, which is identified as the oxygen vacancies [33,34], verifying again that the rich OVs exist in BBI-0.85 ultrathin nanosheets. Oppositely, the absence of this signal in BBI-P sample reveals that there is quite a low concentration of OVs. Combining with the XPS and ESR characterizations above, it is manifested that the concentration of surface oxygen vacancies is rich in the ultrathin BBI-0.85 nanosheets, whereas that is poor in BBI-P sample, providing the prerequisite for investigating the impact of oxygen vacancies on photocatalytic activity in ultrathin BiOBr$_x$I$_{1-x}$ solid solution structure.

UV-vis DRS was employed to investigate the optical properties of BBI-x nanosheets. In Fig. 4a, the absorption edge of BBI-0.85 nanosheets occurs a remarkable red-shifting as compared to that of BB,

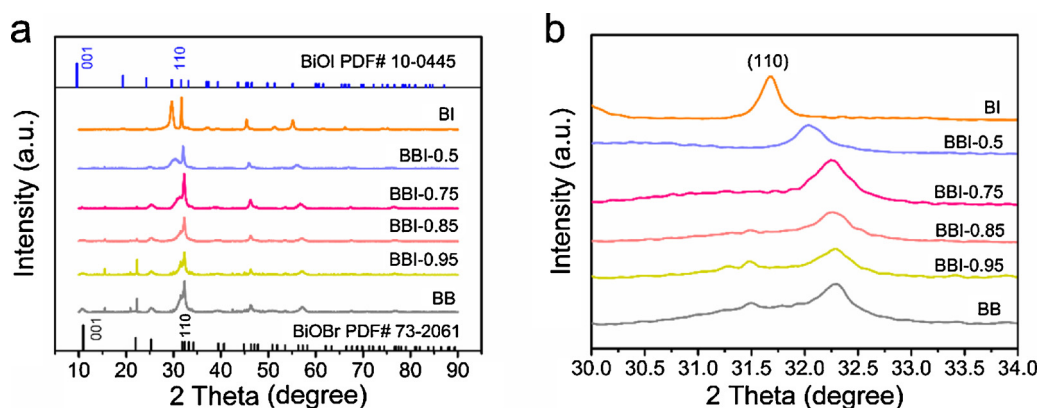**Fig. 1.** (a) XRD patterns of BBI-x samples (x = 1, 0.95, 0.85, 0.75, 0.5, 0). (b) The enlarged XRD patterns with 2θ values from 30° to 34°.

whereas it still smaller than that of BI. This reveals that the formation of solid solution can indeed modulate the capacity of visible light absorption to some extent, which is consistent with the previous reports [6,14]. Meanwhile, the absorption edge of BBI-0.85 also possesses an obvious red-shifting with respect to BBI-P, corresponded to a band gap narrowing and optical absorption enhancement, which is owing to the overlapping of the OVs' electronic states with the semiconductors' band edge [30,35]. The corresponding optical band gap energy (Eg) can be calculated by the following formula [30]:

$\alpha h\nu = A(h\nu-Eg)^{n/2}$, where α, h, ν and A represent the absorption coefficient, Planck constant and light frequency and proportionality,

respectively. And n is equal to 4 resulting from the fundamental absorption of both BiOBr and BiOI are indirect transition between bands. As depicted in Fig. 4b, the optical Eg of BB, BI, BBI-0.85 and BBI-P are estimated to be 2.08, 1.55, 1.65 and 2.12 eV, respectively. Further, to investigate the valence band (VB) of samples, the valence band X-ray photoelectron spectra (VB-XPS) were adopted. As shown in Fig. 4c, the positions of valence band of BB, BI, BBI-0.85 and BBI-P are found to be at 0.76, 0.32, 0.63 and 0.73 eV, respectively. According to the equation of $E_{CB} = E_g-E_{VB}$ [30], the conduction band (CB) edges of BB, BI, BBI-0.85 and BBI-P are calculated to be −1.32, −1.23, −1.02 and −1.39 eV, respectively. Based on the above analysis, the obtained band
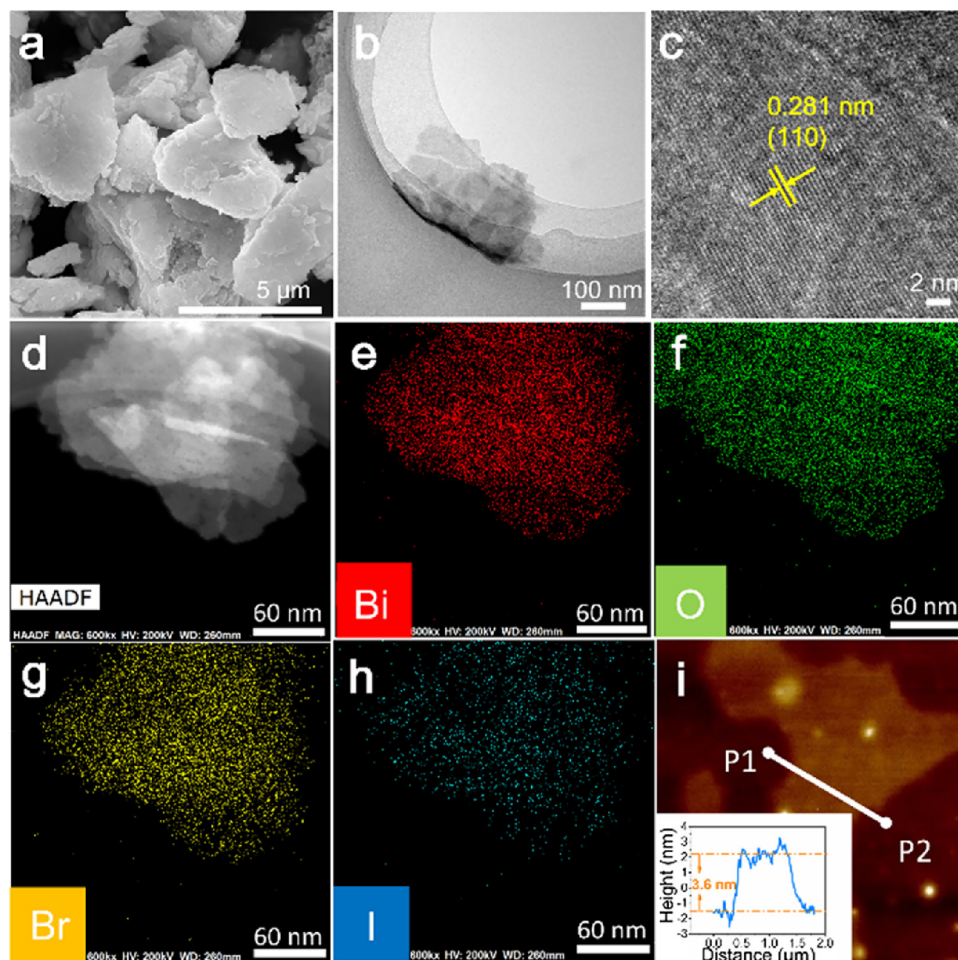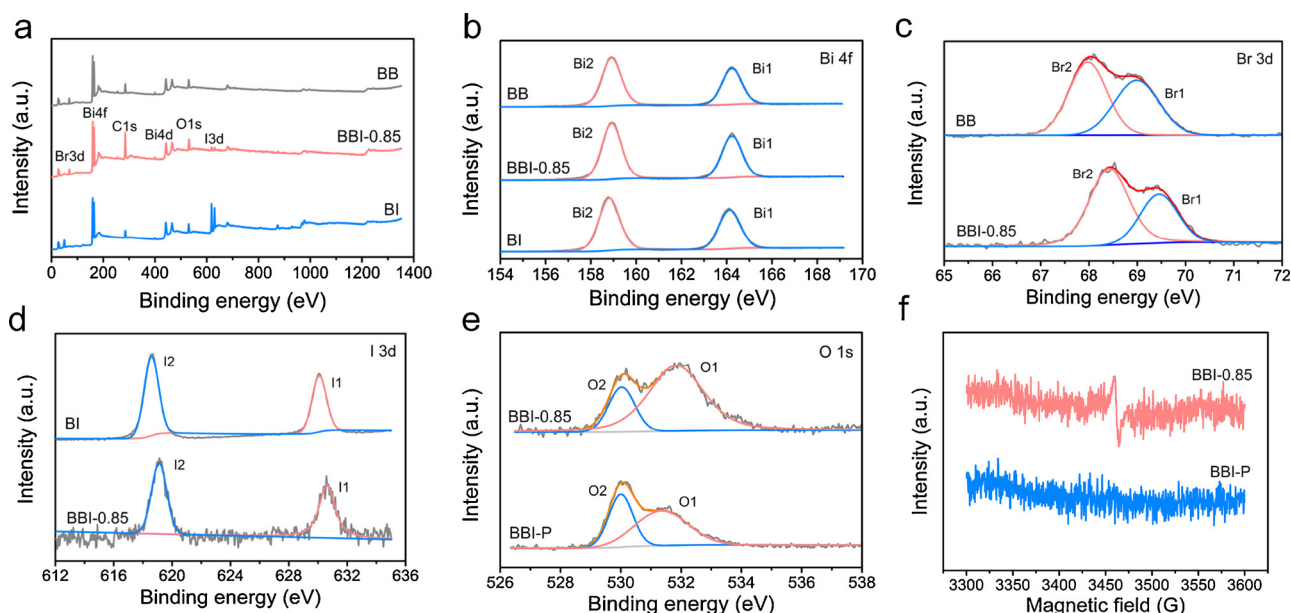

Fig. 2. (a) SEM image of ultrathin BBI-0.85 nanosheets. (b) TEM image of BBI-0.85. (c) High-magnification of TEM image of BBI-0.85. (d–h) HAADF-STEM image (d) and corresponding EDS mapping images (e–h) of BBI-0.85. (i) AFM image of BBI-0.85 and the corresponding height profile shown in the inset of (i).

Fig. 3. XPS spectra of BB, BBI-0.85 and BI nanosheets : (a) survey, (b) Bi 4f spectrum, (c) Br 3d spectrum and (d) I 3d spectrum. (e) The high resolution XPS spectra of O 1 s and (f) ESR spectra of as-prepared ultrathin BBI-0.85 nanosheets, using BBI-P as a reference.

positions of these samples were plotted using the slab model, with the results shown in Fig. 4d. It is intuitively indicated that BBI-0.85 has a narrower band gap than BB, and the VB position of BBI-0.85 is higher than BI simultaneously, unveiling that BBI-0.85 possesses the virtue of enhanced visible-light absorption via a narrow Eg, as well as elevated oxidizing ability though a high VB position [18,36]. Moreover, the Eg of BBI-0.85 is smaller than BBI-P, demonstrating that rich OVs is also conducive to improve the visible-light absorptive capacity [37].

3.2. Photocatalytic activity

4-chlorophenol (4-CP) photodegradation was used as a model reaction to evaluate the photoactivities of the as-prepared samples. 4-CP was chosen for two main reasons: (i) it exhibits no visible light absorption, excluding the effect of photosensitization during the photocatalytic process; (ii) 4-CP has been detected in wastewater and drinking water extensively, which possesses toxicity to the aquatic organism and ability to bioaccumulate in organisms [22,30].
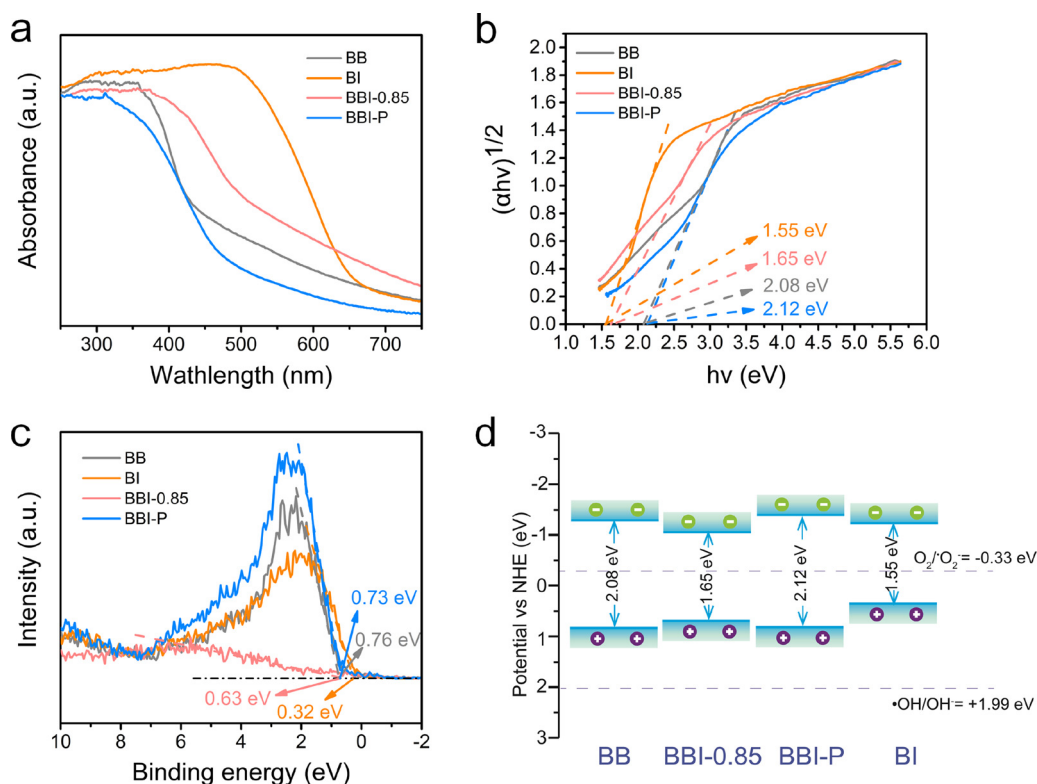
Fig. 4. (a) UV–vis diffuse reflection spectra of BB, BI, BBI-0.85 and BBI-P. (b) The bandgap value, estimated by a related curve of $(\alpha h\nu)^{1/2}$ versus photon energy plotted. (c) VB-XPS spectra of BB, BI, BBI-0.85 and BBI-P. (d) The band position schematic of BB, BI, BBI-0.85 and BBI-P.
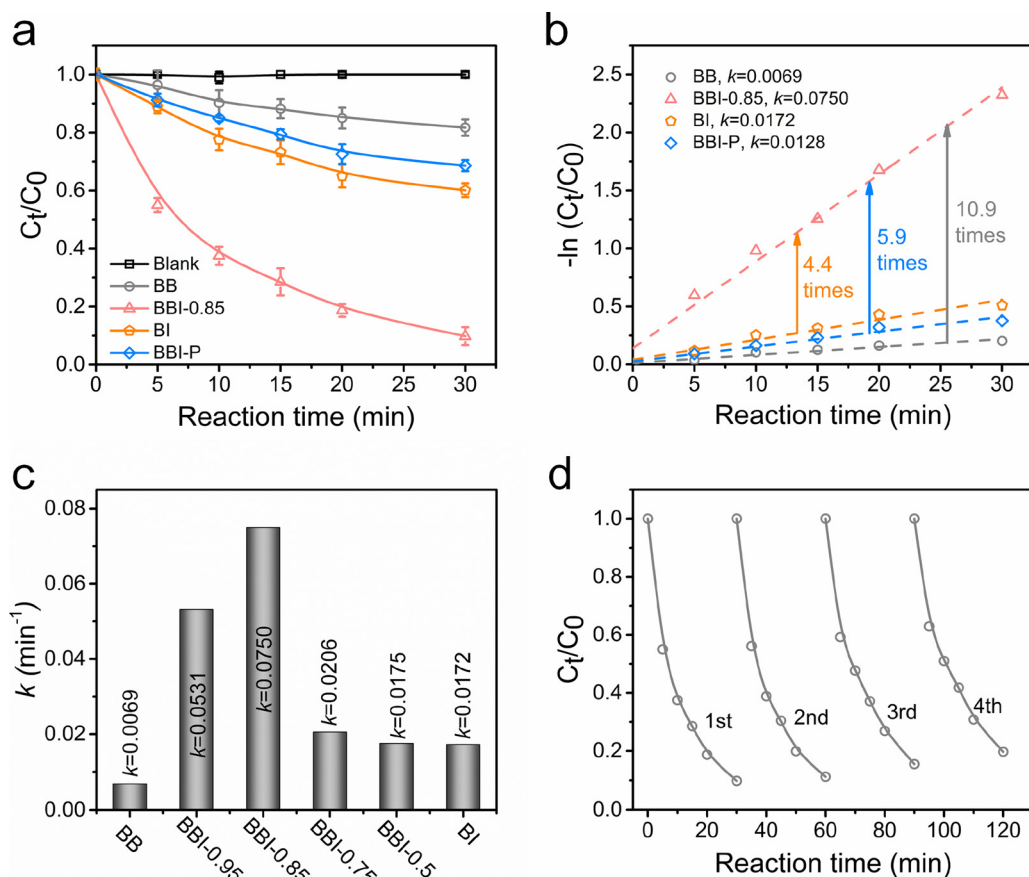
Fig. 5. (a) Photocatalytic degradation of 4-CP under visible light irradiation over different samples. (b) Pseudo first-order kinetic fitting and the determined apparent rate constants (k). (c) k of the series of BBI-x samples in the degradation of 4-CP under visible light irradiation. (d) 4-CP removal in the repeated tests over the as-prepared BBI-0.85.

Without irradiation (Fig. S2), it can be observed that the 4-CP and catalyst suspensions reach absorption-desorption equilibrium at 10 min, and all samples show a small adsorption ability of 4-CP. Under visible light irradiation, as depicted in Fig. 5a, the blank experiment reveals that 4-CP is barely decomposed without photocatalysts. The degradation ratio of 4-CP is 18.2% and 39.1% for pure ultrathin BB and BI nanosheets within 30 min irradiation, respectively. In contrast, the photodegradation activity of as-prepared ultrathin BBI-0.85 solid solution nanosheets is significantly enhanced, and 90.2% of 4-CP can be degraded after 30 min irradiation. It is worthy of note that the atom ratio of Br to I in BBI-0.85 and BBI-P is same, however, the photodegradation efficiency of ultrathin BBI-0.85 sample with rich OVs is distinct superior to that of BBI-P (31.4%), which possesses poor OVs. Besides, the formation dynamics of Cl^- over different photocatalysts were detected (Fig. S3), and among them, the BBI-0.85 sample exhibited highest concentration of Cl^-, also confirming its highest photocatalytic performance. These results imply that the solid solution structure and surface OVs are both conducive to promote photocatalytic performance. In other words, constructing ultrathin solid solution enables the photoactivity to be improved significantly.

Meanwhile, the pseudo first-order linear relationship is revealed by the plots of $-\ln(C_t/C_0)$ vs irradiation time (t), as shown in Fig. 5b. The apparent reaction rate constant (k) of ultrathin BBI-0.85 nanosheet is calculated as $0.0750\,min^{-1}$, which is 4.4, 5.9 and 10.9 times greater than that of BI ($k = 0.0172\,min^{-1}$), BBI-P ($k = 0.0128\,min^{-1}$) and BB nanosheets ($k = 0.0069\,min^{-1}$), respectively. To further assess the optimal mole ratio of Br to I in solid solution, a series of ultrathin BBI-x (x = 1, 0.95, 0.85, 0.75, 0.5 and 0) nanosheets were fabricated and their photodegradation curves and corresponding apparent reaction rate constant (k) were shown in Figs. S9 and 5c, respectively. It can be found that the best value of x is 0.85, and lower or higher x value cannot obtain the best photocatalytic activity. Moreover, the

recyclability and physicochemical stability of the ultrathin BBI-0.85 nanosheets in the degradation of 4-CP are must be considered. The as-prepared BBI-0.85 photocatalyst was isolated from the reaction solution via centrifugation, and reused in the next cycle. In Fig. 5d, the recycling experiment is performed over BBI-0.85, indicating that after four cycles of repeated use, a 4-CP degradation efficiency of 80.3% is still obtained. And, the physicochemical properties of the reused BBI-0.85 nanosheets have been characterized by TEM and XRD images (Fig. S10), and no obvious variations are found in them. The above characterization suggests that the as-prepared ultrathin BBI-0.85 nanosheet can be considered as a relatively stable photocatalyst, and the slight activity loss might be attributed to the slightly decrease of OV concentration (Fig. S11 and Table S1), which decreases from 78.2% in fresh BBI-0.85 to 70.7% in used BBI-0.85 nanosheets. Besides, other persistence organic contaminants, such as bisphenol analogues (BPA, BPF and BPS) and sulfonamides (SDZ and SMZ), can also be degraded efficiently (Fig. S12), verifying the universal applicability of BBI-0.85. More outstanding, BPA and BPF can be entirely removed within 15 min visible-light irradiation.

3.3. Photocatalytic mechanism in the BBI-0.85 system

ESR measurements and typical scavenger tests were employed to evaluate the main oxidative species during the photodegradation process. Fig. 6a and b reveals that no ESR signals of $DMPO-\cdot O_2^-$ adduct and $DMPO-\cdot OH$ adduct are detected in the dark, while the six characteristic peaks of $DMPO-\cdot O_2^-$ and four characteristic peaks of $DMPO-\cdot OH$ species can be obviously observed under visible light irradiation in BBI-0.85 dispersion [38], confirming that $\cdot O_2^-$ and $\cdot OH$ radicals are both produced in the photodegradation process over BBI-0.85 ultrathin nanosheets. Further, as shown in Fig. 6c and d, both of $\cdot O_2^-$ and $\cdot OH$ signal intensities of BBI-0.85 are distinctly stronger than those of BB, BI
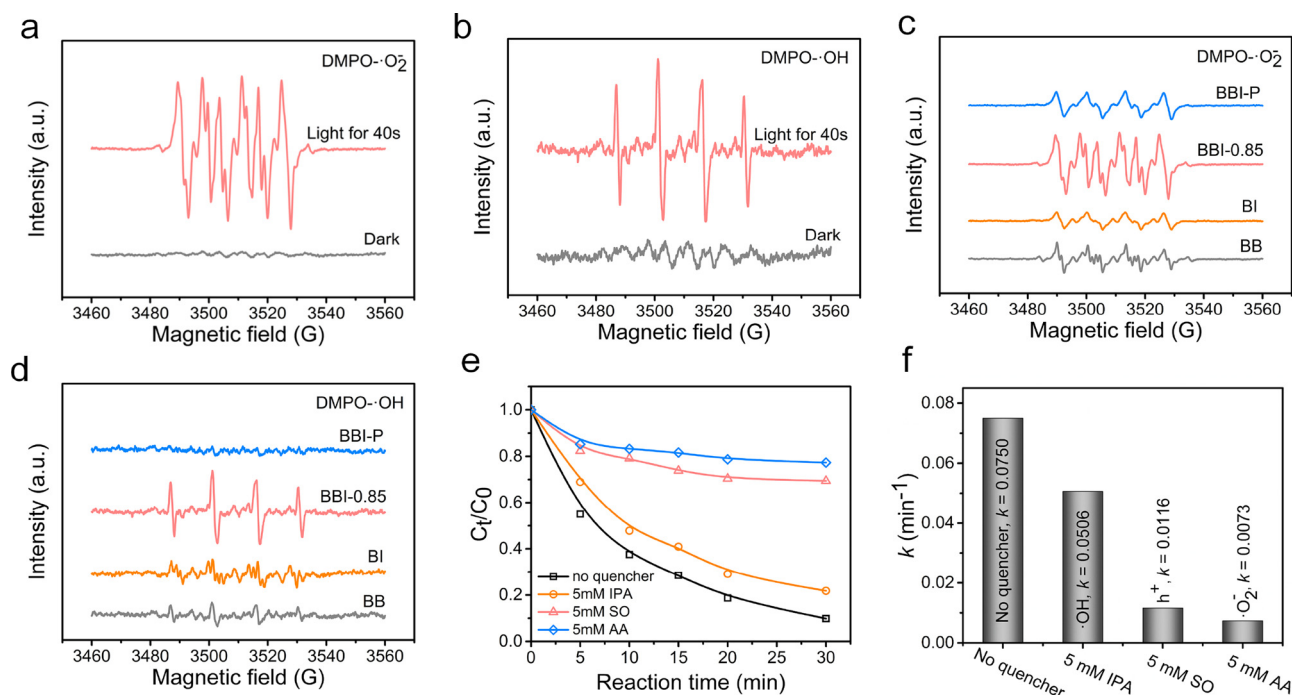
Fig. 6. (a–b) The ESR spectra of DMPO-·O_2^- (a) and DMPO-·OH (b) in the presence of BBI-0.85 ultrathin nanosheets under dark and visible light irradiation for 40s, respectively. (c–d) The ESR spectra of DMPO-·O_2^- (c) and DMPO-·OH (d) over different samples under visible light irradiation for 40s, respectively. (e) Photocatalytic degradation of 4-CP over BBI-0.85 ultrathin nanosheets under visible light irradiation with different scavengers. (f) Pseudo first-order kinetic fitting and the determined apparent rate constants (k) with different quenchers.

and BBI-P after visible light irradiation for 40s, which is consistent with the results of photodegradation efficiency. Meanwhile, the different active species trapping experiments for the degradation of 4-CP over the ultrathin BBI-0.85 nanosheets were also carried out, and during these experiments, we adopted isopropanol (IPA) as the scavenger of ·OH radicals, ascorbic acid (AA) as the scavenger of ·O_2^- radicals, and sodium oxalate (SO) as the scavenger of holes (h^+) [30]. Fig. 6e shows that when 5 mM IPA was added into the reaction solution, the removal efficiency of 4-CP is slightly decreased, which is from 90.2% to 78.2%. In contrast, when 5 mM AA and 5 mM SO were added into the reaction solution, the degradation efficiency of 4-CP are significantly inhibited from 90.2% to 22.7% and 31.6%, respectively. Fig. 6f suggests the corresponding apparent rate constants (k) with different quenchers. The above experiment results manifest that ·O_2^- and h^+ are the major active species in the photocatalytic process of BBI-0.85, while the ·OH radicals make a minor contribution to it.

It is generally accepted that the high surface area, good light absorption capability, appropriate valence and conduction band energies and high separation efficiency of electron-hole pairs are beneficial for the performance of photocatalysts [7,39]. Therefore, several characterizations have been employed systematically to explore the origination of the superior photoactivity of BBI-0.85 nanosheets.

First, the BET surface areas of the catalysts including BB, BI, BBI-0.85 and BBI-P were investigated, as shown in Fig. 7a. It is found that ultrathin BBI-0.85 sample has the highest surface area (89.52 $m^2 g^{-1}$), which is slightly higher that of BBI-P (78.06 $m^2 g^{-1}$), BI (75.49 $m^2 \cdot g^{-1}$) and BB (70.40 $m^2 \cdot g^{-1}$). Generally, the higher surface area makes a contribution to providing more active sites, bringing out the enhanced photocatalytic performance. In order to provide the relationship between the intrinsic photoreactivity and surface area intuitively, apparent reaction rate constant (k) was normalized to the surface area, referred to k_s. As shown in Table 1, BBI-0.85 nanosheet still has a remarkably high photoreactivity with $k_s = 1.676 \times 10^{-3}$ $min^{-1} \cdot L \cdot m^{-2}$ after the normalization of surface area, which is 8.6, 5.1 and 3.7 folds greater than that of BB (0.196 $\times$ 10^{-3} $min^{-1} \cdot L \cdot m^{-2}$), BBI-P (0.328 $\times 10^{-3}$

$min^{-1} \cdot L \cdot m^{-2}$) and BI (0.456 $\times 10^{-3}$ $min^{-1} \cdot L \cdot m^{-2}$), respectively, indicating that the contribution of surface area is extremely weak, and therefore it can be ruled out from the cause of observed excellent photoreactivity.

Second, the above DRS results (Fig. 4a) demonstrate that the addition of I mole ratio in $BiOBr_xI_{1-x}$ can enhance the photoabsorption performance effectively, and with x value decreases, the photoabsorption performance increases gradually, as shown in Figs. S13 and 4a. On the other hand, as depicted in Fig. 4d, as x value increases, the potential of VBM gradually increases, resulting in the higher oxidation capacity of the photogenerated holes [18,40]. Hence, from the two aspects above, the excellent photoactivity of BBI-0.85 is owing to achieving the balance, which acquires superior light absorption capability and sufficient oxidation capacity simultaneously. Furthermore, the photoabsorption performance of ultrathin BBI-0.85 with rich OVs is obviously enhanced with respect to BBI-P with poor OVs, suggesting that the existence of oxygen vancacies is also conducive to the excellent photoactivity of BBI-0.85. Taken together, the formation of solid solution and rich OVs contribute to reinforcing the visible light absorption capability and oxidation capacity of VBM to some extent, which is possibly to be one of the reasons for the preeminent photocatalytic performance of BBI-0.85.

Then, to investigate the actual separation and transportation behaviors of the photoexcited charges in these samples, the photoluminescence (PL) and photoelectrochemical analyses were carried out. As presented in Fig. 7b, compared with ultrathin BB and BI nanosheets, the ultrathin BBI-0.85 shows distinct quenching of the PL intensity with an excitation wavalength of 365 nm, indicating that the photoinduced charge recombination is substantially inhibited with the formed solid solution. Meanwhile, the PL peak of BBI-0.85 is lower than that of BBI-P, suggesting that OVs can further induce more effective separetion of photoinduced carriers, remarkably affecting the lifetime of the carriers and thus enhancing the photocatalytic activity. Fig. 7c records the transient photocurrent responses of the catalysts under visible light irradiation. Among all of the samples, BBI-0.85 shows the largest photocurrent density, revealing less recombination and longer lifetime of
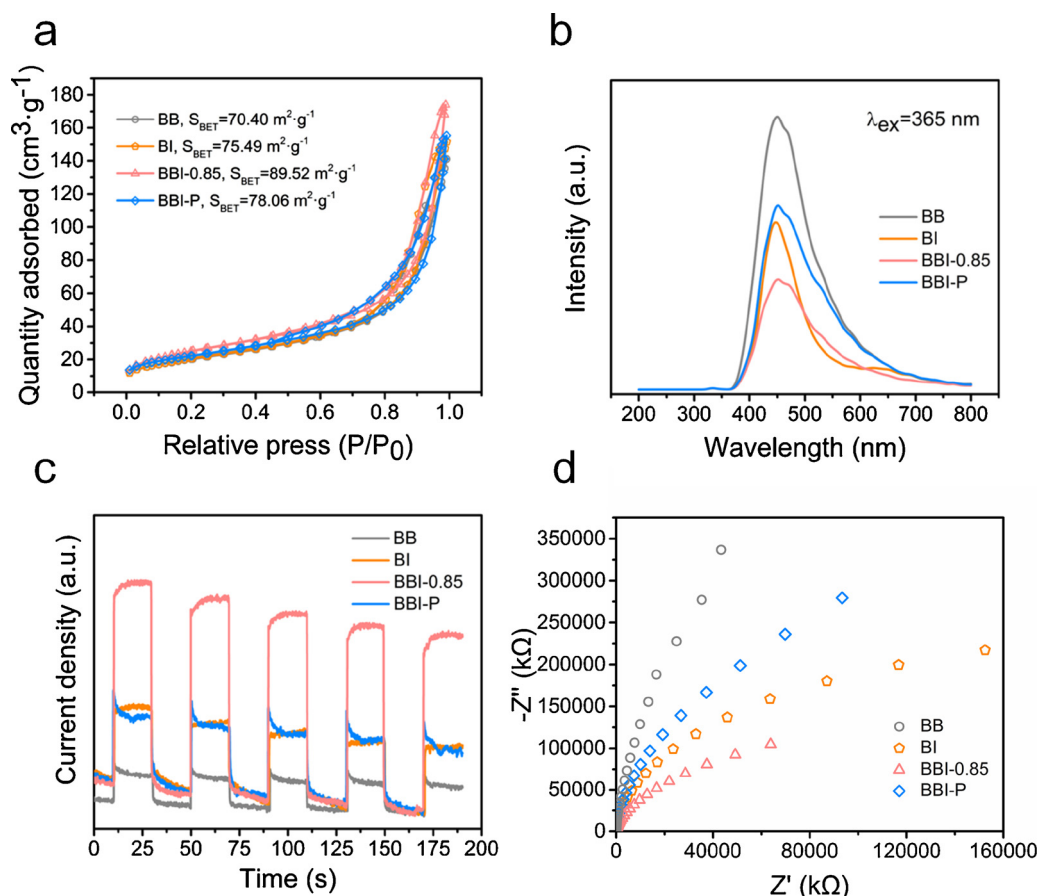
Fig. 7. (a) N_2 adsorption–desorption isotherms, (b) photoluminescence spectra, (c) transient photocurrent responses and (d) electrochemical impedance spectra of the samples under visible light irradiation.

Table 1
Physicochemical properties of the samples.

Sample description	Reaction rate constant[a] k ($\times 10^{-3}\,min^{-1}$)	Surface area[b] ($m^2\,g^{-1}$)	Normalized reaction rate constants[c] k_s ($\times 10^{-3}\,min^{-1}\,L\,m^{-2}$)
BB	6.9	70.40	0.196
BI	17.2	75.49	0.456
BBI-0.85	75.0	89.52	1.676
BBI-P	12.8	78.06	0.328

[a] Apparent reaction rate constants (k) of 4-CP photodegradation on BBI-x samples were calculated based on the pseudo-first-order model.
[b] Surface areas were calculated by Brunauer–Emmett–Teller theory.
[c] k_s denoted the rate constant (k) normalized to surface area and catalyst concentration, k_s = k·(catalyst concentration × surface area)$^{-1}$[30].

photoinduced charges than those of others, which unveils that charge separation efficiency can be enhanced by introducing solid solution structure and OVs [41]. Further, the electrochemical impedance spectra (EIS) of the samples have also been measured and compared (Fig. 7d). Normally, the smaller radius in an EIS Nyquist is, the better charge transfer ability would be, which would impede the recombination of photogenerated charge carriers [42]. As presented in Fig. 7d, obviously, BBI-0.85 has the smallest radius with respect to other samples, indicating much lower electron transfer resistance than BB, BI and BBI-P, and therefore, defines higher charge transfer efficiency [41,43]. Accordingly, the enhancement of separation efficiency of photoinduced electron-hole pairs (e^--h^+) ought to be another origin of excellent photoactivity of ultrathin BBI-0.85 nanosheets.

Further, DFT calculation were performed to further clarify how

oxygen vacancies and solid solution affect the visible light absorption and e^--h^+ separation efficiency in BBI-0.85 system. As presented in Fig. 8, the Fermi energy level is at 0 eV, and the conduction band and valence band are located above and below the Fermi level, respectively. In Fig. 8a and b, both BBI-0.85 and BBI-P contain the indirect band gap, owing to the location of valence band maximum (VBM) and conduction band minimum (CBM) at different k-point [44]. Remarkably, there is a sub-band induced by OVs in ultrathin BBI-0.85, and this defect level appears near the Fermi level and forms the VBM of BBI-0.85, which are consistent with previous investigations [9,45,46]. Correspondingly, the band gap is calculated to be 1.062 eV, while that of BBI-P is 2.085 eV, which are both slightly lower than the DRS results, as a consequence of the well-known GGA-PBE underestimation [47]. This result reveals that the introduction of oxygen vacancies can narrow the band gap and increase the photoabsorption, which are in good agreement with DRS results. Further, the partial density of states (DOS, Fig. 9c) shows that the OV gap state is composed of Bi 6p state, which is mainly from the Bi atoms nearest to the OVs. Owing to the absence of O atoms, the Bi atoms bonded to the lost O atom become electropositive and accordingly, act as a capture center for photoinduced electron (e^-), demonstrating that the recombination of e^--h^+ is restrained [9].

Meanwhile, Fig. 8c also depicts that, in BBI-0.85, the VB is mainly independent of the involvement of Br 4p, I 5p and O 2p states, slightly hybridized with Bi 6 s state, and the CB mainly consisted of Bi 6p state. By contrast, as shown in Fig. S14, the VB is mainly contributed by the hybridization of Br 4p and O 2p states, and I 5p and O 2p states in BB and BI system, respectively. Importantly, due to the hybridization of the different halogen np states in $BiOBr_xI_{1-x}$, the photoinduced hole (h^+) mobility decreases a lot [9]. Whereas the electron mobility of $BiOBr_xI_{1-x}$ is not affected by this hybridization and is similar to that of the
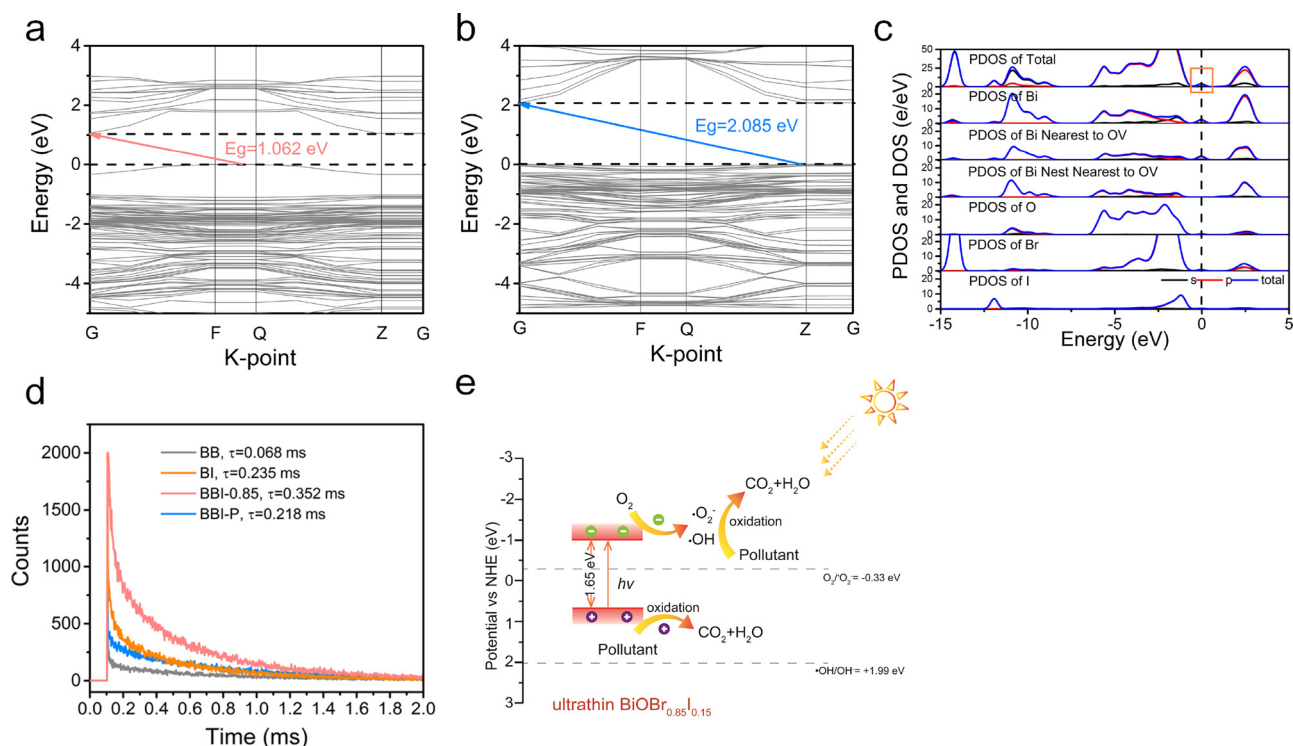
Fig. 8. Band structure of ultrathin BBI-0.85 with rich OVs (a), and bulk BBI-P with poor OVs (b). (c) Corresponding partial density of states of ultrathin BBI-0.85. (d) The time-resolved PL spectra of BB, BI, BBI-0.85 and BBI-P. (e) Schematic illustration of the visible light photocatalytic degradation pollutants over OVs-rich ultrathin BBI-0.85 nanosheets.

corresponding pure BiOBr and BiOI [9]. Consequently, $BiOBr_xI_{1-x}$ structures possess considerably lower e^--h^+ recombination rates, and thereby, much higher photocatalytic efficiencies, which is in correspondence with our experiments results. Similarly, when different amounts of Br are substituted by I in the $BiOBr_xI_{1-x}$, the hybridizations of halogen np states are changed, and as a consequence, the discrepant e^--h^+ separation efficiencies are obtained [9]. This could be confirmed by PL spectra of BBI-x samples (Fig. S15), and among these samples, the PL peak of BBI-0.85 is lower than others, suggesting its excellent photoactivity.

Additionally, time-resolved PL spectra of BB, BI, BBI-0.85 and BBI-P were investigated to provide more information about the charge carriers` lifetime, as shown in Fig. 8d. The emission decay spectra of these samples were fitted well to a double-exponential function ($I = A_1 e^{-t/\tau_1} + A_2 e^{-t/\tau_2}$), exhibiting two radiative lifetimes (τ_1 and τ_2) with different fitting coefficients (A_1 and A_2), which is summarized in Table S2. Moreover, an overall comparison of the emission decay behavior is deduced by the intensity-average lifetimes (τ) through the following equation [32]:

$$\tau = \frac{A_1\tau_1^2 + A_2\tau_2^2}{A_1\tau_1 + A_1\tau_2}$$

The calculation average lifetime of BBI-0.85 is 0.352 ms, which is longer than that of BB (0.068 ns), BI (0.235 ms) and BBI-P (0.218 ms), respectively. The average PL lifetime can be regarded as a crude yet rational measure for quantitative evaluating the separation efficiency of photogenerated charges [48]. In the present case, the effective electron transport and charge separation efficiency are achieved in ultrathin BBI-0.85 nanosheets, manifesting that solid solution and OVs co-enhance the photocatalytic performance of BBI-0.85.

Based on all of the aforementioned results, the photocatalytic mechanism of OVs-rich BBI-0.85 ultrathin nanosheets can be proposed as follows: On one hand, the $BiOBr_{0.85}I_{0.15}$ solid solution structure can tailor the electronic structure, thereby narrowing the Eg, as well as

acquiring relative high VB position with a strong oxidizing h^+, and inhibiting the recombination of e^--h^+. On the other hand, the defect level induced by rich OVs can expand the absorbing edge and act as a capture center for e^- to facilitate the separation efficiency of e^--h^+, thus enhancing the photocatalytic activity. As shown in Fig. 8e, the pairs of electrons and holes are photogenerated on the surface of BBI-0.85 under visible light irradiation, and then the electrons are motivated into the CB, and the holes are remained in VB. The h^+ cannot directly oxidize the adsorbed H_2O molecules to ·OH radicals because their potential for h^+ is lower than $E(·OH/OH^-)$ ($+1.99$ eV vs NHE, pH = 7) [30,49]. Instead, the h^+ can directly oxidize 4-CP to carbon dioxide and water. Meanwhile, due to the potential for e^- is more negative than $E(O_2/·O_2^-)$ (-0.33 eV vs NHE, pH = 7) [30,49], the ·O_2^- radicals begin to produce via the reduction of dissolved O_2 by e^-. After that, the ·OH is generated from ·O_2^- with the assistance of e^-. Accordingly, the active species of h^+, ·O_2^-, and ·OH can continuously decompose 4-CP. Therefore, it can be concluded that the synergistic effect between solid solution structure and oxygen vacancies promotes the capacity of light absorption, injects sufficient potential into photoinduced holes, facilitates the efficient separation of photogenerated electron-hole pairs with a prolonged charge lifetime, and thus accelerates the photocatalytic oxidation process.

Besides, in this study, nine intermediates including phenol ($m/z = 93$), hydroquinone ($m/z = 109$), maleic acid ($m/z = 115$), crotonyl alcohol ($m/z = 71$), 4-chlorocatechol ($m/z = 143$), hydroxyquinol ($m/z = 125$), hydrobenzoquinone ($m/z = 123$) and 2,4,6-trichlorophenol (2,4,6-TCP, $m/z = 195$) were detected by mass spectrometry analyses during the visible-light photocatalytic degradation of 4-CP ($m/z = 127$) over BBI-0.85 for 30 min (Fig. S16–S23). Specially, hydroquinone, a well-known chemical substance suffers from instability due to rapid oxidation to 1,4-benzoquinone. And 1,4-benzoquinone cannot be detected by UPLC-MS, because it is not able to ionize into ions [30]. According to these results, the possible transformation pathways have been proposed as exhibited in Fig. 9 [50–52]. Dechlorination and hydroxylation could be the most prominent pathways supporting by the
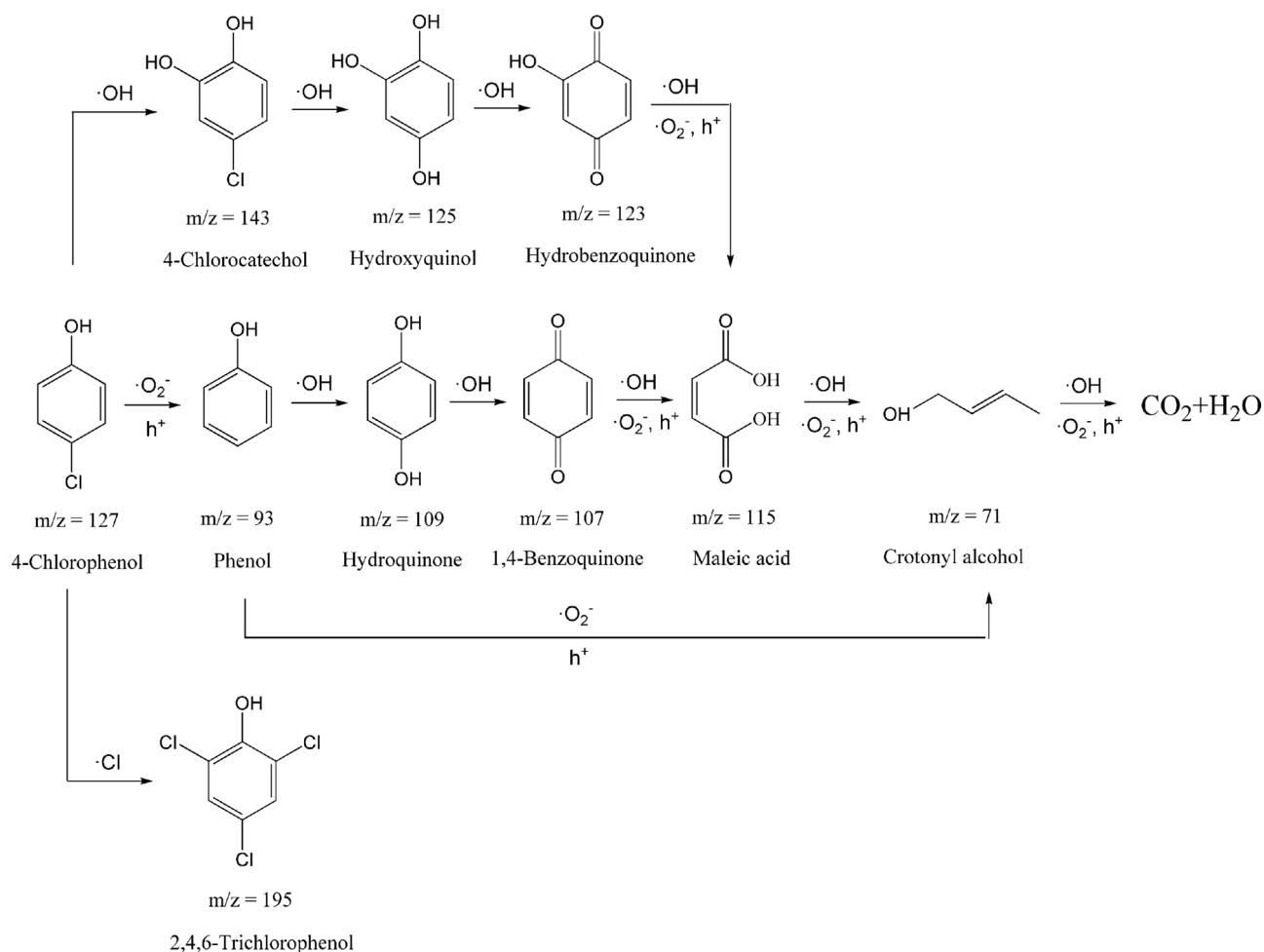
Fig. 9. Proposed degradation pathways of 4-chlorophenol (4-CP) over BBI-0.85 within 30 min.

main intermediates such as maleic acid and crotonyl alcohol. Trace of 2,4,6-TCP may derive from the reaction between chlorine radical (·Cl, formed during dechlorination of 4-CP) and 4-CP [51].

4. Conclusion

In this work, ultrathin $BiOBr_xI_{1-x}$ solid solution photocatalysts with rich oxygen vacancies were successfully constructed through a facile solvothermal method. Benefiting from the extended visible light absorption range, the high VB position, and efficient charge separation arising from the synergistic effect between solid solution and oxygen vacancies, the $BiOBr_xI_{1-x}$ exhibited superior photocatalytic activities in 4-CP degradation. As an optimal ratio of $BiOBr_{0.85}I_{0.15}$, over 90% of 4-CP was decomposed within 30 min of visible light irradiation, and the rate constant of $BiOBr_{0.85}I_{0.15}$ was 4.4, 10.9 and 5.9 times greater than that of pristine BiOI, BiOBr and oxygen vacancy-poor $BiOBr_{0.85}I_{0.15}$ nanoplates, respectively. This study exposes the promising prospect of coupling defect with solid solution via the ultrathin solid solution strategy on promoting photocatalysis, and may have potentials to be extended to other applications, such as molecular oxygen activation, electrocatalysis and supercapacitors.

Conflict of Interest

The authors declare no conflict of interest.

Appendix A. Supplementary data

Supplementary material related to this article can be found, in the online version, at doi:https://doi.org/10.1016/j.apcatb.2018.05.029.

References

[1] H. Wang, L. Zhang, Z. Chen, J. Hu, S. Li, Z. Wang, J. Liu, X. Wang, Chem. Soc. Rev. 43 (2014) 5234–5244.
[2] D. Ravelli, D. Dondi, M. Fagnoni, A. Albini, Chem. Soc. Rev. 38 (2009) 1999–2011.
[3] Y. Nosaka, A.Y. Nosaka, Chem. Rev. 117 (2017) 11302–11336.
[4] L. Li, J. Yan, T. Wang, Z.J. Zhao, J. Zhang, J. Gong, N. Guan, Nat. Commun. 6 (2015) 5881.
[5] R.S. Sprick, J.X. Jiang, B. Bonillo, S. Ren, T. Ratvijitvech, P. Guiglion, M.A. Zwijnenburg, D.J. Adams, A.I. Cooper, J. Am. Chem. Soc. 137 (2015) 3265–3270.
[6] X. Zhang, C.Y. Wang, L.W. Wang, G.X. Huang, W.K. Wang, H.Q. Yu, Sci. Rep. 6 (2016) 22800.
[7] Y. Zhao, Y. Zhao, G.I.N. Waterhouse, L. Zheng, X. Cao, F. Teng, L.Z. Wu, C.H. Tung, D. O'Hare, T. Zhang, Adv. Mater. 29 (2017) 1703828.
[8] X. Tao, Y. Zhao, S. Mu, S. Wang, R. Li, C. Li, Adv. Energy Mater. (2017) 1701392.
[9] H. Zhang, L. Liu, Z. Zhou, Phys. Chem. Chem. Phys. 14 (2012) 1286–1292.
[10] F. Chen, Q. Yang, Y. Wang, J. Zhao, D. Wang, X. Li, Z. Guo, H. Wang, Y. Deng, C. Niu, G. Zeng, Appl. Catal. B: Environ. 205 (2017) 133–147.
[11] X. She, J. Wu, H. Xu, J. Zhong, Y. Wang, Y. Song, K. Nie, Y. Liu, Y. Yang, M.-

T.F. Rodrigues, R. Vajtai, J. Lou, D. Du, H. Li, P.M. Ajayan, Adv. Energy Mater. 7 (2017) 1700025.

[12] J. Ran, T.Y. Ma, G. Gao, X.-W. Du, S.Z. Qiao, Energy Environ. Sci. 8 (2015) 3708–3717.

[13] Y. Liu, W.J. Son, J. Lu, B. Huang, Y. Dai, M.H. Whangbo, Chemistry 17 (2011) 9342–9349.

[14] Y. Bai, L. Ye, T. Chen, P. Wang, L. Wang, X. Shi, P.K. Wong, Appl. Catal. B: Environ. 203 (2017) 633–640.

[15] K. Ji, J. Deng, H. Zang, J. Han, H. Arandiyan, H. Dai, Appl. Catal. B: Environ. 165 (2015) 285–295.

[16] X. Xu, R. Lu, X. Zhao, S. Xu, X. Lei, F. Zhang, D.G. Evans, Appl. Catal. B: Environ. 102 (2011) 147–156.

[17] X. Zhang, L.W. Wang, C.Y. Wang, W.K. Wang, Y.L. Chen, Y.X. Huang, W.W. Li, Y.J. Feng, H.Q. Yu, Chemistry 21 (2015) 11872–11877.

[18] H. Xu, X. Han, Q. Tan, X. He, S. Qi, Catalysts 7 (2017) 153.

[19] Y. Lei, G. Wang, P. Guo, H. Song, Appl. Surf. Sci. 279 (2013) 374–379.

[20] G. Zhang, S. Sun, W. Jiang, X. Miao, Z. Zhao, X. Zhang, D. Qu, D. Zhang, D. Li, Z. Sun, Adv. Energy Mater. 7 (2017) 1600932.

[21] H. Yu, R. Shi, Y. Zhao, T. Bian, Y. Zhao, C. Zhou, G.I.N. Waterhouse, L.Z. Wu, C.H. Tung, T. Zhang, Adv. Mater. 29 (2017) 1605148.

[22] G. Zhang, Z. Hu, M. Sun, Y. Liu, L. Liu, H. Liu, C.-P. Huang, J. Qu, J. Li, Adv. Funct. Mater. 25 (2015) 3726–3734.

[23] C. Dong, C. Lian, S. Hu, Z. Deng, J. Gong, M. Li, H. Liu, M. Xing, J. Zhang, Nat. Commun. 9 (2018) 1252.

[24] W. Fang, M. Xing, J. Zhang, J. Photochem. Photobiol. C: Photochem. Rev. 32 (2017) 21–39.

[25] Y. Liu, H. Cheng, M. Lyu, S. Fan, Q. Liu, W. Zhang, Y. Zhi, C. Wang, C. Xiao, S. Wei, B. Ye, Y. Xie, J. Am. Chem. Soc. 136 (2014) 15670–15675.

[26] H. Li, J. Li, Z. Ai, F. Jia, L. Zhang, Angew. Chem. Int. Ed. 57 (2018) 122–138.

[27] Q. Hao, R. Wang, H. Lu, Ca. Xie, W. Ao, D. Chen, C. Ma, W. Yao, Y. Zhu, Appl. Catal. B: Environ. 219 (2017) 63–72.

[28] J. Di, J. Xia, M. Ji, S. Yin, H. Li, H. Xu, Q. Zhang, H. Li, J. Mater. Chem. A 3 (2015) 15108–15118.

[29] L. Kong, Z. Jiang, H.H. Lai, R.J. Nicholls, T. Xiao, M.O. Jones, P.P. Edwards, J. Catal. 293 (2012) 116–125.

[30] Q. Wang, W. Wang, L. Zhong, D. Liu, X. Cao, F. Cui, Appl. Catal. B: Environ. 220 (2018) 290–302.

[31] Y. Zheng, T. Zhou, X. Zhao, W.K. Pang, H. Gao, S. Li, Z. Zhou, H. Liu, Z. Guo, Adv. Mater. 29 (2017) 1700396.

[32] J. Wang, Y. Xia, H. Zhao, G. Wang, L. Xiang, J. Xu, S. Komarneni, Appl. Catal. B: Environ. 206 (2017) 406–416.

[33] J. Hou, S. Cao, Y. Wu, F. Liang, Y. Sun, Z. Lin, L. Sun, Nano Energy 32 (2017) 359–366.

[34] C. Mao, H. Cheng, H. Tian, H. Li, W. Xiao, H. Xu, J. Zhao, L. Zhang, Appl. Catal. B: Environ. 228 (2018) 87–96.

[35] H. Li, J. Shi, K. Zhao, L. Zhang, Nanoscale 6 (2014) 14168–14173.

[36] P. Xia, B. Zhu, J. Yu, S. Cao, M. Jaroniec, J. Mater. Chem. A 5 (2017) 3230–3238.

[37] J. Wang, Z. Wang, B. Huang, Y. Ma, Y. Liu, X. Qin, X. Zhang, Y. Dai, ACS Appl. Mater. Interfaces 4 (2012) 4024–4030.

[38] Y. Hong, Y. Jiang, C. Li, W. Fan, X. Yan, M. Yan, W. Shi, Appl. Catal. B: Environ. 180 (2016) 663–673.

[39] Y. He, L. Zhang, B. Teng, M. Fan, Environ. Sci. Technol. 49 (2015) 649–656.

[40] F. Tian, H. Zhao, Z. Dai, G. Cheng, R. Chen, Ind. Eng. Chem. Res. 55 (2016) 4969–4978.

[41] D. Zhang, Y. Guo, Z. Zhao, Appl. Catal. B: Environ. 226 (2018) 1–9.

[42] Y. Hou, F. Zuo, A. Dagg, P. Feng, Nano Lett. 12 (2012) 6464–6473.

[43] W. Wang, S. You, X. Gong, D. Qi, B.K. Chandran, L. Bi, F. Cui, X. Chen, Adv. Mater. 28 (2016) 270–275.

[44] A.M. Ganose, M. Cuff, K.T. Butler, A. Walsh, D.O. Scanlon, Chem. Mater. 28 (2016) 1980–1984.

[45] H. Zhang, Y. Yang, Z. Zhou, Y. Zhao, L. Liu, J. Phys. Chem. C 118 (2014) 14662–14669.

[46] X. Zhang, G. Ji, Y. Liu, X. Zhou, Y. Zhu, D. Shi, P. Zhang, X. Cao, B. Wang, Phys. Chem. Chem. Phys. 17 (2015) 8078–8086.

[47] J. Zhang, S. Wageh, A. Al-Ghamdi, J. Yu, Appl. Catal. B: Environ. 192 (2016) 101–107.

[48] P. Yang, H. Ou, Y. Fang, X. Wang, Angew. Chem. Int. Ed. 56 (2017) 3992–3996.

[49] X. Hu, J. Tian, Y. Xue, Y. Li, H. Cui, ChemCatChem 9 (2017) 1511–1516.

[50] M. Humayun, Y. Qu, F. Raziq, R. Yan, Z. Li, X. Zhang, L. Jing, Environ. Sci. Technol. 50 (2016) 13600–13610.

[51] H. Ji, F. Chang, X. Hu, W. Qin, J. Shen, Chem. Eng. J. 218 (2013) 183–190.

[52] J. Seo, H. Lee, H.-J. Lee, M.S. Kim, S.W. Hong, J. Lee, K. Cho, W. Choi, C. Lee, Appl. Catal. B: Environ. 225 (2018) 487–495.